

# Global climate evolution during the last deglaciation

Peter U. Clark<sup>a,1</sup>, Jeremy D. Shakun<sup>b,1</sup>, Paul A. Baker<sup>c</sup>, Patrick J. Bartlein<sup>d</sup>, Simon Brewer<sup>e</sup>, Ed Brook<sup>a</sup>, Anders E. Carlson<sup>f,g</sup>, Hai Cheng<sup>h,i</sup>, Darrell S. Kaufman<sup>j</sup>, Zhengyu Liu<sup>a,k</sup>, Thomas M. Marchitto<sup>l</sup>, Alan C. Mix<sup>a</sup>, Carrie Morrill<sup>m</sup>, Bette L. Otto-Bliesner<sup>n</sup>, Katharina Pahnke<sup>o</sup>, James M. Russell<sup>p</sup>, Cathy Whitlock<sup>q</sup>, Jess F. Adkins<sup>r</sup>, Jessica L. Blois<sup>g,s</sup>, Jorie Clark<sup>a</sup>, Steven M. Colman<sup>t</sup>, William B. Curry<sup>u</sup>, Ben P. Flower<sup>v</sup>, Feng He<sup>g</sup>, Thomas C. Johnson<sup>t</sup>, Jean Lynch-Stieglitz<sup>w</sup>, Vera Markgraf<sup>x</sup>, Jerry McManus<sup>x</sup>, Jerry X. Mitrovica<sup>b</sup>, Patricio I. Moreno<sup>y</sup>, and John W. Williams<sup>z</sup>

<sup>a</sup>College of Earth, Ocean, and Atmospheric Sciences, Oregon State University, Corvallis, OR 97331; <sup>b</sup>Department of Earth and Planetary Sciences, Harvard University, Cambridge, MA 02138; <sup>c</sup>Division of Earth and Ocean Sciences, Duke University, Durham, NC 27708; <sup>d</sup>Department of Geography, University of Oregon, Eugene, OR 97403; <sup>e</sup>Department of Geology, University of Utah, Salt Lake City, UT 84112; <sup>f</sup>Department of Geoscience, University of Wisconsin, Madison, WI 53706; <sup>g</sup>Center for Climatic Research, University of Wisconsin, Madison, WI 53706; <sup>h</sup>Institute of Global Environmental Change, Xi'an Jiaotong University, Xi'an 710049, China; <sup>i</sup>Department of Geology and Geophysics, University of Minnesota, Minneapolis, MN 55455; <sup>j</sup>School of Earth Sciences and Environmental Sustainability, Northern Arizona University, Flagstaff, AZ 86011; <sup>k</sup>Laboratory for Ocean-Atmosphere Studies, School of Physics, Peking University, Beijing 100871, China; <sup>l</sup>Institute of Arctic and Alpine Research, University of Colorado, Boulder, CO 80309; <sup>m</sup>National Oceanic and Atmospheric Administration National Climatic Data Center, Boulder, CO 80305; <sup>n</sup>Climate and Global Dynamics Division, National Center for Atmospheric Research, Boulder, CO 80307; <sup>o</sup>Department of Geology and Geophysics, University of Hawaii, Honolulu, HI 96822; <sup>p</sup>Department of Geological Sciences, Brown University, Providence, RI 02912; <sup>q</sup>Department of Earth Sciences, Montana State University, Bozeman, MT 97403; <sup>r</sup>Division of Geological and Planetary Sciences, California Institute of Technology, Pasadena, CA 91125; <sup>s</sup>Department of Geography, University of Wisconsin, Madison, WI 53706; <sup>t</sup>Large Lakes Observatory and Department Geological Sciences, University of Minnesota, Duluth, MN 55812; <sup>u</sup>Department of Geology and Geophysics, Woods Hole Oceanographic Institution, Woods Hole, MA 02543; <sup>v</sup>College of Marine Science, University of South Florida, St. Petersburg, FL 33701; <sup>w</sup>School of Earth and Atmospheric Sciences, Georgia Institute of Technology, Atlanta, GA 30332; <sup>x</sup>Lamont-Doherty Earth Observatory, Palisades, NY 10964; and <sup>y</sup>Institute of Ecology and Biodiversity and Department of Ecological Sciences, Universidad de Chile, Santiago 1058, Chile

Edited by Mark H. Thieme, University of California at San Diego, La Jolla, CA, and approved January 4, 2012 (received for review October 10, 2011)

**Deciphering the evolution of global climate from the end of the Last Glacial Maximum approximately 19 ka to the early Holocene 11 ka presents an outstanding opportunity for understanding the transient response of Earth's climate system to external and internal forcings. During this interval of global warming, the decay of ice sheets caused global mean sea level to rise by approximately 80 m; terrestrial and marine ecosystems experienced large disturbances and range shifts; perturbations to the carbon cycle resulted in a net release of the greenhouse gases CO<sub>2</sub> and CH<sub>4</sub> to the atmosphere; and changes in atmosphere and ocean circulation affected the global distribution and fluxes of water and heat. Here we summarize a major effort by the paleoclimate research community to characterize these changes through the development of well-dated, high-resolution records of the deep and intermediate ocean as well as surface climate. Our synthesis indicates that the superposition of two modes explains much of the variability in regional and global climate during the last deglaciation, with a strong association between the first mode and variations in greenhouse gases, and between the second mode and variations in the Atlantic meridional overturning circulation.**

**D**uring the interval of global warming from the end of the Last Glacial Maximum (LGM) approximately 19 ka to the early Holocene 11 ka, virtually every component of the climate system underwent large-scale change, sometimes at extraordinary rates, as the world emerged from the grips of the last ice age (Fig. 1). This dramatic time of global change was triggered by changes in insolation, with associated changes in ice sheets, greenhouse gas concentrations, and other amplifying feedbacks that produced distinctive regional and global responses. In addition, there were several episodes of large and rapid sea-level rise and abrupt climate change (Fig. 2) that produced regional climate signals superposed on those associated with global warming. Considerable ice-sheet melting and sea-level rise occurred after 11 ka, but otherwise the world had entered the current interglaciation with near-pre-Industrial greenhouse gas concentrations and relatively stable climates. Here we synthesize well-dated, high-resolution ocean and terrestrial proxy records to describe regional and global patterns of climate change during this interval of deglaciation.

Between the LGM and present, seasonal insolation anomalies arising from the combined effects of eccentricity, precession, and obliquity were generally opposite in sign between hemispheres (Fig. 2C), whereas variations in annual-average insolation were symmetrical about the equator. At the LGM, seasonal insolation

was similar to present, whereas subsequent changes in obliquity and perihelion caused Northern-Hemisphere seasonality to reach a maximum in the early Holocene.

CO<sub>2</sub> concentrations started to rise from the LGM minimum approximately 17.5 ± 0.5 ka (1). The onset of the CO<sub>2</sub> rise may have lagged the start of Antarctic warming by 800 ± 600 years (1), but this may be an overestimate (2). CO<sub>2</sub> levels stabilized from approximately 14.7–12.9 ka, and then rose again from about 12.9–11.7 ka, reaching near-interglacial maximum levels shortly thereafter. CH<sub>4</sub> concentrations also began to rise starting at approximately 17.5 ka, with a subsequent abrupt increase at 14.7 ka, an abrupt decrease at about 12.9 ka, followed by a rise at approximately 11.7 ka (3). Changes in N<sub>2</sub>O concentrations appear to follow changes in CH<sub>4</sub> (4). The combined variations in radiative forcing due to greenhouse gases (GHGs) is dominated by CO<sub>2</sub>, but abrupt changes in CH<sub>4</sub> and N<sub>2</sub>O modulate the overall structure, accentuating the rapid increase at 14.7 ka and causing a slight reduction from 12.9–11.7 ka (Fig. 2D).

Freshwater forcing of the Atlantic meridional overturning circulation (AMOC) is commonly invoked to explain past and possibly future abrupt climate change (5, 6). During the last deglaciation, the AMOC was likely affected by variations in moisture transport across Central America (7), salt and heat transport from the Indian Ocean (8), freshwater exchange across the Bering Strait (9), and the flux of meltwater and icebergs from adjacent ice sheets (6). The first two factors largely represent feedbacks on AMOC variability. Freshwater exchange across the Bering Strait began with initial submergence of the Strait during deglacial sea-level rise. Highly variable fluxes from ice-sheet melting and calving and routing of continental runoff (Fig. 2E–I) also directly forced the

Author contributions: P.U.C., J.D.S., Z.L., and B.L.O.-B. designed research; P.U.C., J.D.S., and J.X.M. performed research; P.U.C., J.D.S., A.E.C., H.C., Z.L., B.L.O.-B., J.F.A., J.L.B., J.C., S.M.C., W.B.C., B.P.F., F.H., T.C.J., J.L.-S., V.M., J.M., P.I.M., and J.W.W. analyzed data; and P.U.C., J.D.S., P.A.B., P.J.B., S.B., E.B., A.E.C., D.S.K., T.M.M., A.C.M., C.M., K.P., J.M.R., and C.W. wrote the paper.

The authors declare no conflict of interest.

This article is a PNAS Direct Submission.

<sup>1</sup>To whom correspondence may be addressed. E-mail: clarkp@onid.orst.edu or shakun@fas.harvard.edu.

See Author Summary on page 7140 (volume 109, number 19).

This article contains supporting information online at [www.pnas.org/lookup/suppl/doi:10.1073/pnas.1116619109/-DCSupplemental](http://www.pnas.org/lookup/suppl/doi:10.1073/pnas.1116619109/-DCSupplemental).

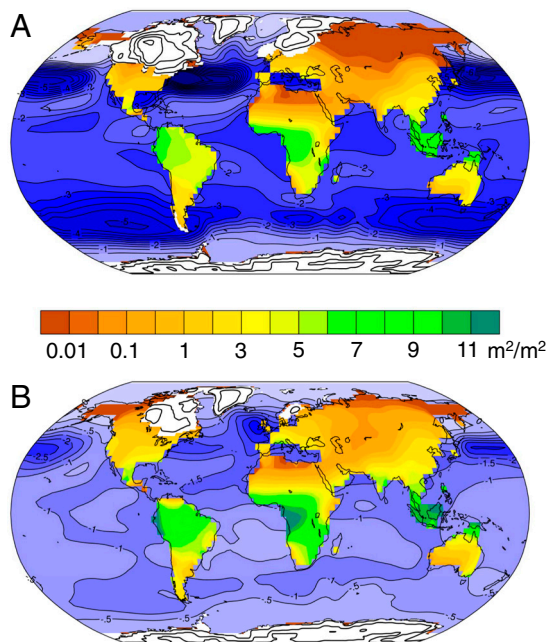


**Fig. 1.** (A) Climate simulation of the Last Glacial Maximum 21,000 y ago using the National Center for Atmospheric Research Community Climate System Model, version 3.0 (141). Sea-surface temperatures are anomalies relative to the control climate. Also shown are continental ice sheets (1,000-m contours) (149) and leaf-area index simulated by the model (scale bar shown). (B) Same as A except for 11 ka.

AMOC, but uncertainties in the sources of several key events remain (*SI Appendix*).

## Results

**Sea-Surface Temperatures.** We compiled 69 high-resolution proxy sea-surface temperature (SST) records spanning 20–11 ka that provide broad coverage of the global ocean (*SI Appendix*). Our evaluation of SST reconstructions from regional ocean basins suggests that warming trends are smallest at low latitudes (1–3 °C) and higher at higher latitudes (3–6 °C) (*SI Appendix*, Fig. S2). In any given basin, however, there is considerable variation among the specific proxy reconstructions as well as between the different proxies. We thus use Empirical Orthogonal Function (EOF) analysis to extract the dominant common modes of regional and global SST variability from the dataset (*Methods* and *SI Appendix*). Two orthogonal modes explain 78% of deglacial SST variability. The first EOF mode exhibits a globally near-uniform spatial pattern (*SI Appendix*, Fig. S4). Its associated principal component (PC1) displays a two-step warming pattern from approximately 18–14.3 and 12.8–11.0 ka, with an intervening plateau (Fig. 3A). The second EOF mode exhibits a more complex spatial pattern (*SI Appendix*, Fig. S4), but its associated PC2 is dominated by millennial-scale oscillations with decreases during the Oldest and Younger Dryas events separated by an increase during the Bølling–Allerød period (Fig. 3B).

We also calculate the leading PCs for different latitudinal bands. PC1 explains an increasing fraction of regional variance moving southward from the northern extratropics (59%) to the southern extratropics (79%), indicating that the climate records have more in common further to the south (*SI Appendix*, Fig. S5). The regional PC1 for the northern extratropics includes millennial-scale variability similar to the global SST PC2, whereas PC1s for the tropics and southern extratropics exhibit two-step warming patterns, similar to the global SST PC1.

**Intermediate-Water Changes.** During the LGM, there was a chemical divide at approximately 2–2.5 km water depth in the North Atlantic that separated shallower, nutrient-poor Glacial North

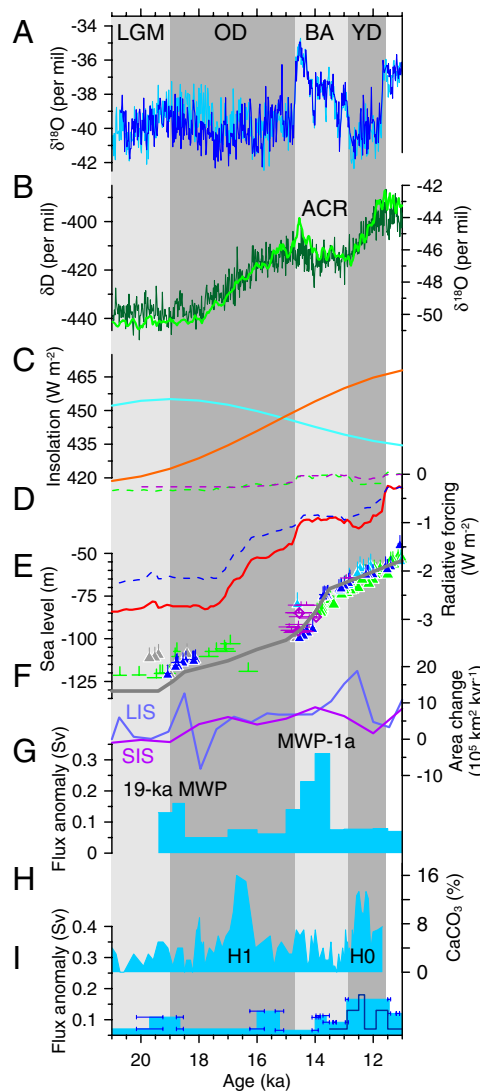


**Fig. 2.** Climate records and forcings during the last deglaciation. The oxygen-isotope ( $\delta^{18}\text{O}$ ) records from Greenland Ice Sheet Project Two (GISP2) (150) (dark-blue line) and Greenland Ice Core Project (GRIP) (151) (light-blue line) Greenland ice cores shown in (A) (placed on the GICC05 timescale; ref. 57) document millennial-scale events that correspond to those first identified in northern European floral and pollen records. LGM, Last Glacial Maximum; OD, Oldest Dryas; BA, Bølling–Allerød; ACR, Antarctic Cold Reversal; YD, Younger Dryas. (B) Oxygen-isotope ( $\delta^{18}\text{O}$ ) record from European Project for Ice Coring in Antarctica (EPICA) Dronning Maud Land (152) (dark-green line) and deuterium ( $\delta\text{D}$ ) record from Dome C (45) (light-green line) Antarctic ice cores, placed on a common timescale (2). (C) Midmonth insolation at 65°N for July (orange line) and at 65°S for January (light-blue line) (153). (D) The combined radiative forcing (red line) from  $\text{CO}_2$  (blue dashed line),  $\text{CH}_4$  (green dashed line), and  $\text{N}_2\text{O}$  (purple dashed line) relative to preindustrial levels.  $\text{CO}_2$  is from EPICA Dome C ice core (1) on the GICC05 timescale,  $\text{CH}_4$  is from GRIP ice core (154) on the GICC05 timescale, and  $\text{N}_2\text{O}$  is from EPICA Dome C (155) and GRIP (156) ice cores on the GICC05 timescale. Greenhouse gas concentrations were converted to radiative forcings using the simplified expressions in ref. 157. The  $\text{CH}_4$  radiative forcing was multiplied by 1.4 to account for its greater efficacy relative to  $\text{CO}_2$  (158). (E) Relative sea-level data from Bonaparte Gulf (green crosses) (159), Barbados (gray and dark-blue triangles) (160), New Guinea (light-blue triangles) (161, 162), Sunda Shelf (purple crosses) (163), and Tahiti (green triangles) (164). Also shown is eustatic sea level (gray line) (165). (F) Rate of change of area of Laurentide Ice Sheet (LIS) (166) and Scandinavian Ice Sheet (SIS) (*SI Appendix*). (G) Freshwater flux to the global oceans derived from eustatic sea level in E. (H) Record of ice-rafted detrital carbonate from North Atlantic core VM23-81 identifying times of Heinrich events 1 and 0 (167). (I) Freshwater flux associated with routing of continental runoff through the St. Lawrence and Hudson rivers (filled blue time series) with age uncertainties (168). Also shown is time series of runoff through the St. Lawrence River during the Younger Dryas (solid blue line) (142).

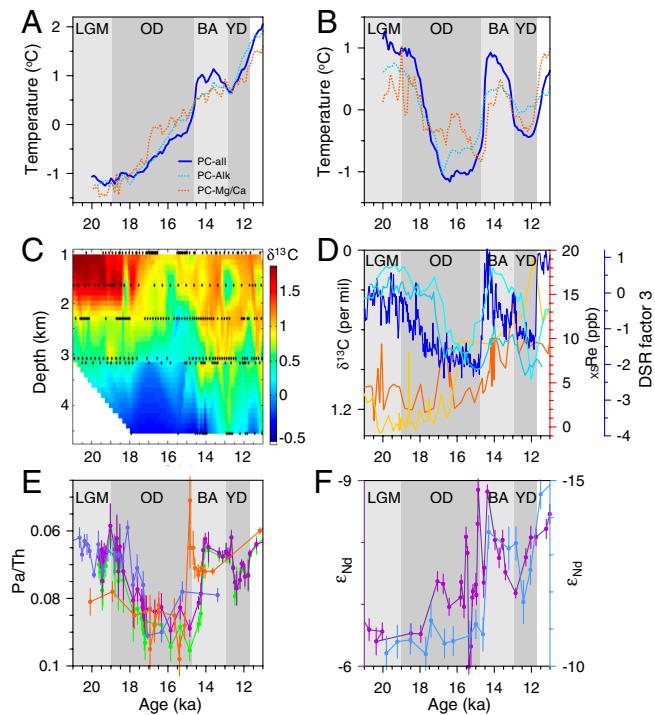


**Fig. 3.** (A) Principal component (PC) 1 based on all of the SST records (solid blue line). PC1s based only on alkenone (dashed light-blue line) and Mg/Ca records (dashed orange line) are also shown. The percentage of variance explained by PC1 is 49%, by PC1 (Mg/Ca) is 59%, and by PC1 ( $U^K_{37}$ ) is 64%. (B) PC2 based on all of the SST records (solid blue line). PC2s based only on alkenone (dashed light-blue line) and Mg/Ca records (dashed orange line) are also shown. The percentage of variance explained by PC2 is 29%, by PC2 (Mg/Ca) is 13%, and by PC2 ( $U^K_{37}$ ) is 15%. (C) Temporal evolution of  $\delta^{13}C$  in the North Atlantic basin reconstructed from data shown by black diamonds based on a depth transect of six marine cores (10, 12, 26, 169–171). (D) Proxy records of intermediate-depth waters from the Arabian Sea and Pacific Ocean. Cyan line is  $\delta^{13}C$  record from the Arabian Sea (20), sky blue line is five-point running average of  $\delta^{13}C$  record from the SW Pacific Ocean (19), blue line is diffuse spectral reflectance (factor 3 loading) (a proxy of organic carbon) from the North Pacific (24), yellow and orange lines are records of excess Re (a proxy of dissolved oxygen) from the southeast Pacific (21). (E) Pa/Th records from the North Atlantic Ocean (27, 28, 172). (F)  $\epsilon_{Nd}$  records from the North Atlantic (14) (blue line) and south Atlantic (173) (purple line). Abbreviations are as in Fig. 2.

Atlantic intermediate water (GNAIW) from more nutrient-rich deep water (10, 11) (Fig. 2C). Low nutrients at intermediate depths likely reflect increased formation of well-ventilated GNAIW and a reduced northward extent of nutrient-rich Antarctic intermediate water (AAIW) (11). The nutrient content of intermediate waters increased during the Oldest and Younger Dryas events (Fig. 3C), indicating a possible reduction in the volume of GNAIW (12). Neodymium isotope data ( $\epsilon_{Nd}$ ) indicate that there may also have been an incursion of a Southern Ocean water mass similar to that of present-day AAIW (13), or alternatively that southern-sourced deep waters already filling the deep North Atlantic basin (14) shoaled to intermediate depth. Additional evidence for increased northward extent of AAIW at these times comes from elevated radiocarbon reservoir ages in North Atlantic planktonic foraminifera (15) and low, Southern Ocean-like  $\Delta^{14}C$  at mid-depth in the North Atlantic (16) and on the Brazil margin (17).

Deep-intermediate  $\delta^{13}C$  gradients increased in the LGM equatorial Pacific, suggesting stronger or lower-nutrient AAIW influence (18). In the southwest Pacific (19) and the Arabian Sea (20),  $\delta^{13}C$  values were lower at intermediate-depth sites during the LGM, increased approximately 17.5 ka, decreased again during the Bølling–Allerød, and subsequently increased during the

Younger Dryas (Fig. 3D). The increases in  $\delta^{13}C$  may reflect an increased influence of glacial AAIW (19, 20), although changes in the preformed  $\delta^{13}C$  of the intermediate water cannot be excluded. In contrast, intermediate-depth sites in the southeast Pacific document evidence for an expanded depth range of a more-oxygenated AAIW during the LGM followed by stepwise reduction in oxygen content between 17 and 11 ka (21) (Fig. 3D). The results from the southwest and southeast Pacific on the timing of changes in AAIW thus differ, and additional evidence is needed to resolve whether these two areas were indeed subject to different changes at intermediate-water depth. In the eastern North Pacific, Nd isotope data may record an expansion of AAIW during the Oldest Dryas interval (ca. 18–15 ka) (22), although an alternative forcing from the north is possible.

Along the North American Pacific margin, intermediate-depth  $O_2$  levels were higher than today during the LGM, Oldest Dryas, and the Younger Dryas, and lower than today during the Bølling–Allerød interval and earliest Holocene (23, 24) (Fig. 3D). These changes can be explained by enhanced (decreased) formation of North Pacific intermediate water (NPIW) and/or by reduced (increased) productivity along the North American margin; proxy evidence lends support to both scenarios.

**Deep-Ocean Changes.** During the LGM, increased nutrients in North Atlantic deep waters likely resulted from a northward and upward expansion of Antarctic bottom water at the expense of North Atlantic deep water (NADW) (11). Benthic-planktic radiocarbon differences were slightly higher at the LGM than at present, consistent with overall vigorous circulation, although with greater influence of Antarctic water masses of relatively low preformed  $^{14}C$  associated with incomplete gas exchange with the atmosphere (25). The circulation proxies  $\epsilon_{Nd}$  (Fig. 3F) and  $\Delta^{14}C$  suggest little difference between the Oldest Dryas and the LGM in the deepest North Atlantic (14, 16), whereas  $^{231}Pa/^{230}Th$  and particularly  $\delta^{13}C$  suggest that the net AMOC decreased below LGM strength at nearly all depths during the Oldest Dryas (12, 26–29) (Fig. 3C and E). All tracers of deepwater production indicate renewed production of NADW at the start of the Bølling–Allerød, followed by a subsequent decrease during the Younger Dryas (Fig. 3C, E, and F), although  $\Delta^{14}C$  records suggest a much greater decrease than  $^{231}Pa/^{230}Th$  at this time (16, 27).

Reconstructions of  $\delta^{13}C$  also support the existence of a deep chemical divide in the Indo-Pacific during the LGM, although it was somewhat shallower than in the Atlantic (30). The possibility that a deeper version of NPIW formed in the LGM North Pacific remains uncertain (31). Deep water may have formed in the northwestern Pacific to 3,000-m depth during the Oldest Dryas (32).

The low concentrations of atmospheric  $CO_2$  during the LGM are thought to have been caused by greater storage of carbon in the deep ocean through stratification of the Southern Ocean (33, 34). Southern Ocean deep waters had the lowest  $\delta^{13}C$  values (35) and were the source of the most dense (36) and salty (37) waters in the LGM deep ocean. Release of the sequestered carbon may have occurred due to deep Southern Ocean overturning induced by enhanced wind-driven upwelling (38) and sea-ice retreat (34) associated with times of Antarctic warming, coincident with the Oldest and Younger Dryas cold events in the north (1). There may be a low  $\Delta^{14}C$  signal of this two-pulse release that spread as far as the North Pacific (39) and north Indian (40) oceans via AAIW. Although recent  $\Delta^{14}C$  evidence from the intermediate-depth Brazil margin supports this scenario (17), data from the Chilean and New Zealand margins do not (41, 42). Evidence for a water mass with very low  $\Delta^{14}C$  values in the deepest parts of the ocean is contradictory (43, 44), however, indicating that our understanding of the relationship between deep-ocean circulation, its interaction with the atmosphere, and carbon fluxes is incomplete.

**Polar Regions.** LGM temperatures in East Antarctica were approximately 9–10°C lower than today (45), whereas average LGM temperatures in Greenland were approximately 15°C lower (46). There are also good constraints on the abrupt warmings that occurred in Greenland at the end of the Oldest Dryas (9 ± 3°C) and Younger Dryas (10 ± 4°C) events (47, 48).

Synchronization of Greenland and Antarctic  $\delta D$  and  $\delta^{18}O$  records (49–52) confirmed a north-south antiphasing of hemispheric temperatures (bipolar seesaw) during the last deglaciation (53–55) (Fig. 2). Despite these advances, uncertainties in relative timing of events between Greenland and Antarctic ice-core records remain, and not all records agree on the precise timing of abrupt events. For example, in contrast to the standard bipolar seesaw model, the Law Dome ice-core record indicates that the Antarctic Cold Reversal started before the Bølling (56). Moreover, the stable isotope records in Greenland cores differ during the Oldest Dryas (57), whereas in Antarctica, East Antarctic ice cores and two West Antarctic ice cores have similar patterns that broadly follow the classic seesaw pattern, whereas two other West Antarctic ice cores (Siple Dome and Taylor Dome) suggest a more complicated deglacial record (58, 59). It remains unclear, however, as to whether these latter differences are due to uncertainties in chronology, elevation changes, stratigraphic disturbances, or spatially variable climate changes (59–61).

**Beringia.** During the LGM, proxy records indicate that July temperatures were approximately 4°C lower than present in eastern Beringia (62), whereas central and western Beringia experienced relatively warm summers similar to present (63). Summer temperatures in eastern Beringia began to increase between 17 and 15 ka, with peak warmth reached by the start of the Bølling, and temperatures similar to or warmer than modern during the subsequent Allerød (63). During the Younger Dryas, temperatures were similar or warmer-than-present across most of central Alaska, northeastern Siberia, and possibly the Russian Far East and northern Alaska, whereas southern Alaska, eastern Siberia, and portions of northeastern Siberia cooled (64).

**North America.** During the LGM, eastern North America vegetation was dominated by forests comprised of cold-tolerant conifers that may have formed an open conifer woodland or parkland, including in areas currently occupied by grassland (65–67). The southeastern and northwestern United States supported open forest in areas that are presently closed forest, suggesting colder and drier-than-present conditions (68–70), whereas the American southwest had open forest in areas of present-day steppe and desert, indicating wetter conditions (71–73). Overall, these vegetation changes suggest a steepened latitudinal temperature gradient, southward shift of westerly storm tracks, and a general temperature decrease of at least 5°C, with considerable spatial variability (66, 71, 74–76).

Vegetation changes between 16 and 11 ka closely track millennial-scale climate variability (77) with time lags on the order of 100 y or less (78, 79). Abrupt changes in ecosystem function are also indicated by elevated rates of biomass burning accompanying abrupt warming events at 13.2 ka and at the end of the Younger Dryas (11.7 ka) (80). The highest rates of change in eastern North America are associated with the beginning and end of the Younger Dryas (66, 74). Equally abrupt and synchronous hydrological changes also occurred in the southwest (72, 73), with parallel changes in treeline in the Rocky Mountains (81).

**South America.** Noble gas ratios in fossil groundwater indicate that LGM surface air temperature decreased by 5–6°C relative to modern in the Nordeste of Brazil (7°S) (82). Tropical paleo-precipitation patterns during the LGM indicate that, relative to modern, precipitation was generally less north of the equator (83), greater throughout the South American summer monsoon (SASM) sector

extending from approximately 0 to 30°S (84–86), and less in the east-central Amazon and the Nordeste of Brazil (87).

Little is known about deglacial temperature changes, whereas precipitation changes are reasonably well constrained. In most of the region, wet periods coincide with wet-season insolation maxima that are of opposite sign across the equator, although north-eastern tropical Brazil is an exception because it is antiphased with the SASM region (87). Millennial-scale changes are superimposed on this insolation-driven pattern, with dry events throughout the northern tropics (88, 89) and wet events throughout the southern tropics (84–87, 90–92) during the Oldest and Younger Dryas. These millennial hydrologic responses appear to be of similar magnitude as the response to orbital forcing.

In southern South America, vegetation patterns suggest that LGM climate was colder and drier than at present, and the southern westerly wind belt, with associated rainfall, was shifted northward (40–44°S) or weakened (93, 94). Cold parkland conditions persisted west of the Andes until 17.5 ka between 40 and 44°S and until 15.0 ka between 44 and 47°S, after which climate warmed (95–97). In northern and southern Patagonia, cold steppe-like conditions were present until 13.0 ka east of the Andes, with significant warming after that (98, 99). Vegetation records indicate cooling during the Antarctic Cold Reversal between approximately 15.0 and 12.6 ka (97), but that the region subsequently experienced spatially variable responses through the Younger Dryas (100).

**Europe.** Pollen records indicate that during the LGM, northern Europe was covered by open, steppe-tundra environments (101, 102), whereas southern Europe was covered largely by steppe-grassland and semidesert environments (103), but with mountains providing refugia for most deciduous tree species (104). Climate reconstructions from these records that account for the effects of lower atmospheric CO<sub>2</sub> indicate winter cooling of 5–15°C across Europe, with the greatest cooling in western Europe, and precipitation decreases of as much as 300 to 300–400 mm y<sup>-1</sup> in the west (105).

The termination of the LGM was marked by a slight increase in temperature and precipitation (106–108), followed by a cool and dry stadial from approximately 17.5 to 14.7 ka (i.e., during the Oldest Dryas) when vegetation returned to its glacial state (107). At the onset of the Bølling, temperatures increased rapidly by 3–5°C across western Europe (109), whereas subsequent cooling at the start of the Younger Dryas ranged between 5 and 10°C (110–112). This temperature decrease resulted in a return to grassland communities in the south of Europe and tundra in the north. The Younger Dryas ended abruptly in Europe approximately 11.7 ka with a rapid temperature increase of approximately 4°C, but varied latitudinally, with a greater increase in the north (113).

**Africa.** Several different proxies indicate that, during the LGM, much of Africa was more arid and approximately 4°C colder than present (114, 115). Arid conditions that prevailed across much of North Africa during the Oldest and Younger Dryas (114, 116) extended across the equator to about 10°S in East Africa (117, 118). In northern and eastern equatorial Africa, precipitation began to increase approximately 16 ka, followed by two abrupt increases in precipitation at approximately 15 and 11.5 ka (114, 119–122), which correlate to the abrupt onset of the Bølling and Holocene, respectively, implying intensification of the North African summer monsoon during Northern-Hemisphere interstadials (123, 124).

Although only constrained by a few records, deglacial temperature changes recorded in lakes south of the equator indicate a monotonic increase between approximately 20 and 18 ka, followed by more rapid and larger warming between 18 and 14.5 ka in a pattern similar to that observed in Antarctic ice cores (122, 125, 126). Temperatures subsequently decreased between 14.5 and 12 ka before rapidly increasing to values similar to present at approximately 11 ka (122, 126).

**Monsoonal and Central Asia.** The Asian Monsoon region is comprised of the Indian subdomain, which receives moisture dominantly from the Indian Ocean, and the east Asian subdomain which receives moisture mainly from the Pacific Ocean. Although arid central Asia is beyond the farthest northward extent of the summer monsoon, proxy records from this region delineate the boundary between the monsoon circulation and the midlatitude westerlies as well as document the strength of the winter monsoon associated with the winter Siberian High.

At the LGM, there is evidence for a weak summer monsoon relative to today (127), a stronger winter monsoon (128, 129), and colder, dustier conditions (130, 131). Lakes throughout most of monsoonal and arid central Asia were smaller at the LGM compared to today, probably because of decreased precipitation across the region (132).

A variety of proxy records show a weakened summer monsoon during the Oldest Dryas, a stronger monsoon during the Bølling–Allerød, and a weaker monsoon during the Younger Dryas (127, 131–136). The sequence of events is similar between speleothem records from the Indian and east Asian subdomains, including nearly identical magnitudes of  $\delta^{18}\text{O}$  change (137). Two key differences between the speleothem and Greenland ice-core records are less abrupt transitions in Asia and a strong summer monsoon into the Allerød after Greenland temperature decreased. Relatively slow transitions in Asia also differ from the abrupt shifts in atmospheric methane recorded in ice cores, suggesting a different tropical methane source, such as from high northern latitudes, with a more rapid response (137) or a nonlinear response of Asian methane sources to warming. A lake record of winter monsoon strength from southeast China may indicate an anticorrelation between winter and summer monsoon strength throughout all the deglacial climate events (138).

**Discussion**

We add 97 records to the 69 SST records used previously and recalculate the EOFs to characterize the temporal and spatial

patterns of the leading modes of global climate variability for the 20- to 11-ka interval (*SI Appendix*). In addition to characterizing SST variability as before, we now also characterize variability in regional and global continental temperature and precipitation as well as a composite of global temperature variability (Fig. 4).

The global SST modes remain largely unchanged, with 71% of the variance in the dataset explained by essentially the same two EOFs and PCs (Fig. 4 and *SI Appendix*, Fig. S6). The global continental temperature modes are similarly largely explained by two patterns of variance (70%). As with global SSTs, the first EOF mode for continental temperature exhibits a globally near-uniform spatial pattern with large positive loadings in most records (*SI Appendix*, Fig. S6), and its associated principal component (PC1) displays a similar two-step warming pattern (Fig. 4). The global continental temperature PC2 only differs from the global SST PC2 in having a muted oscillation during the Bølling–Allerød, but is otherwise similar in showing a reduction into the Oldest and Younger Dryas events. Combining ocean and continental temperature records yields global modes that are nearly identical to the global SST modes (Fig. 4).

The majority of the records used for the precipitation EOF analysis are from the tropics and subtropics, with many of these associated with monsoon systems (*SI Appendix*, Fig. S7). The global precipitation EOF1 differs from the global temperature EOF1 in having a more complex spatial pattern (*SI Appendix*, Fig. S7). The associated PC1 also differs in indicating that the initial increase in precipitation lagged the initial increase in the global temperature PC1 by at least 2,000 y, that it had abrupt increases at the end of the Oldest and Younger Dryas events, and that it experienced distinct oscillations corresponding to the Bølling–Allerød and Younger Dryas events (Fig. 4). Other than an approximately 1,000-y delay in the decrease at the start of the Oldest Dryas, PC2 for global continental precipitation is similar to the global temperature PC2.

We also find regional variability for the ocean basins and continents for which we have data as suggested by the factor loading

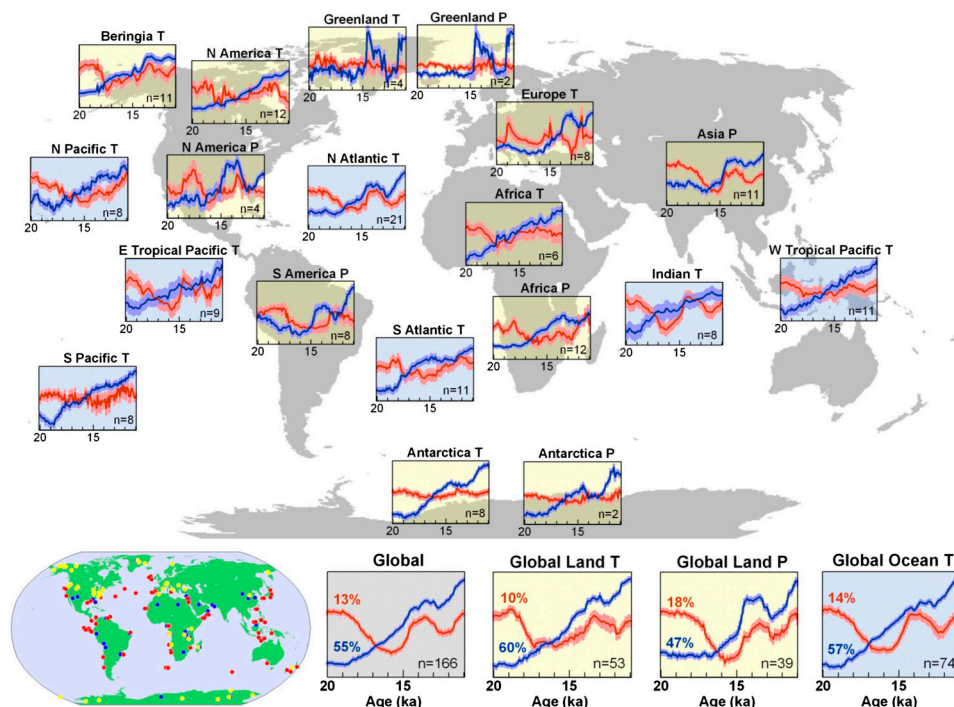


**Fig. 4.** Regional and global principal components (PCs) for temperature (T) and precipitation (P) based on records shown on map in lower left. Red dots on map indicate sites used to constrain ocean sea-surface temperatures, yellow dots constrain continental temperatures, and blue dots constrain continental precipitation. PC1s are shown as blue lines, PC2s as red lines. We used a Monte Carlo procedure to derive error bars ( $1\sigma$ ) for the principal components which reflect uncertainties in the proxy records. All records were standardized to zero mean and unit variance prior to calculating EOFs, which is necessary because the records are based on various proxies and thus have widely ranging variances in their original units (*SI Appendix*).

pattern for the global EOF1 (*SI Appendix, Fig. S6*). Regional SST PC1s suggest that deglacial warming began in the Southern, Indian, and equatorial Pacific oceans, with each regional PC1 also showing a similar two-step structure through the remainder of the deglaciation as identified in the global SST PC1 (Fig. 4). In contrast, regional SST PC1s for the North Atlantic and North Pacific oceans indicate that temperatures began to increase later there and experienced more pronounced millennial-scale variability during the subsequent deglaciation corresponding to the Oldest Dryas-Bølling-Allerød-Younger Dryas events.

The regional continental temperature PC1s also suggest spatially variable patterns of change, whereby Greenland and Europe have a strong expression of millennial-scale events, whereas Beringia, North America, Africa, and Antarctica are more similar to the two-step structure seen in the global land and ocean temperature PC1s (Fig. 4). In contrast, the regional precipitation PC1s for North and South America, Africa, and Asia generally exhibit the millennial-scale structure seen in the global precipitation PC1 (Fig. 4).

Regional PC2s account for a relatively small fraction of the total variance (2–31%) and in some cases are likely insignificant (*SI Appendix*). SST PC2s of most ocean basins display some or all of the millennial-scale structure that characterizes the global SST PC2, with the strongest expression being in the North Atlantic and Indian oceans, but also with a subtle but clear registration in the equatorial Pacific Ocean PC2s (Fig. 4).

Continental regions generally exhibit little coherency with each other in their PC2 patterns. There is little variance preserved in the PC2s for the polar regions (Greenland and Antarctica) (*SI Appendix*), whereas the temperature PC2s for Beringia, North America, Europe, and Africa and precipitation PC2s for North and South America and Africa are all distinct from each other and are thus likely capturing regional variability (Fig. 4). The precipitation PC2 for Asia reveals a clear structure corresponding to the Bølling–Allerød and Younger Dryas events, further indicating the strong influence of millennial-scale climate change on the hydrology of this region.

In conclusion, our synthesis indicates that the superposition of two orthogonal modes explains much of the variability (64–100%) in regional and global climate during the last deglaciation. The nearly uniform spatial pattern of the global temperature EOF1 (*SI Appendix, Fig. S6*) and the large magnitude of the temperature PC1 variance indicate that this mode reflects the global warming of the last deglaciation. Given the large global forcing of GHGs (139), the strong correlation between PC1 and the combined GHG forcing ( $r^2 = 0.97$ ) (Fig. 5A) indicates that GHGs were a major driver of global warming (140).

In contrast, the global temperature PC2 is remarkably similar to a North Atlantic Pa/Th record ( $r^2 = 0.86$ ) that is interpreted as a kinematic proxy for the strength of the AMOC (27) (Fig. 5B). Similar millennial-scale variability is identified in several other proxies of intermediate- and deep-ocean circulation (Fig. 3), identifying a strong coupling between SSTs and ocean circulation. The large reduction in the AMOC during the Oldest Dryas can be explained as a response to the freshwater forcing associated with the 19-ka meltwater pulse from Northern-Hemisphere ice sheets, Heinrich event 1, and routing events along the southern Laurentide Ice Sheet margin (141), whereas the reduction during the Younger Dryas was likely caused by freshwater routing through the St. Lawrence River (142) and Heinrich event 0 (Fig. 5B). The sustained strength of the AMOC following meltwater pulse 1a (Fig. 5B) supports arguments for a large contribution of this event from Antarctica (143). With EOF2 accounting for only 13% of deglacial global climate variability, we conclude that the direct global impact of AMOC variations was small in comparison to other processes operating during the last deglaciation.

The global precipitation EOF1 shows a more complex spatial response than the global temperature EOF1 (*SI Appendix, Fig. S7*), whereas the initial increase in the associated PC1 signif-

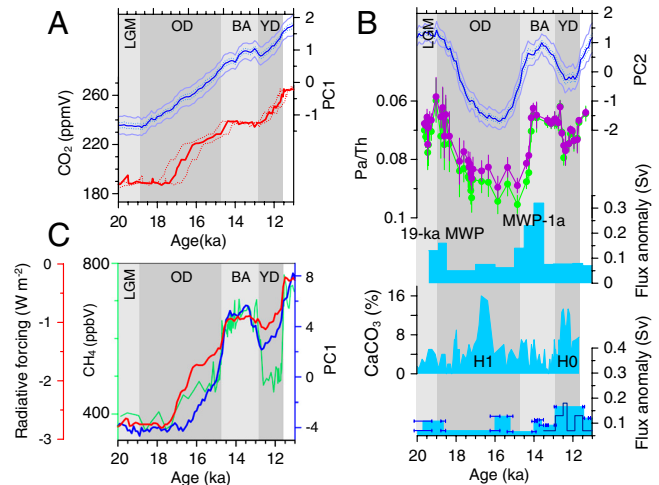


**Fig. 5.** (A) Comparison of the global temperature PC1 (blue line, with confidence intervals showing results of jackknifing procedure for 68% and 95% of records removed) with record of atmospheric CO<sub>2</sub> from EPICA Dome C ice core (red line with age uncertainty) (1) on revised timescale from ref. 2. (B) Comparison of the global temperature PC2 (blue line, with confidence intervals showing results of jackknifing procedure for 68% and 95% of records removed) with Pa/Th record (a proxy for Atlantic meridional overturning circulation) (27) (green and purple symbols). Also shown are freshwater fluxes from ice-sheet meltwater, Heinrich events, and routing events (Fig. 2). (C) Comparison of the global precipitation PC1 (blue line) with record of methane (green line) and radiative forcing from greenhouse gases (red line) (see Fig. 2D). Abbreviations are as in Fig. 2.

icantly lags the initial increase in the global temperature PC1, as well as exhibits greater millennial-scale structure than seen in the global temperature PC1 (Figs. 4 and 5). Insofar as precipitation increases should accompany a warming planet, the approximately 2-ky lag between the initial increase in temperature and precipitation may reflect one or more mechanisms that affect low-latitude hydrology, including the impact of Oldest Dryas cooling (122, 127), a nonlinear response to Northern-Hemisphere forcing by insolation (144) and glacial boundary conditions (145), or interhemispheric latent heat transports (146). This response may then have been modulated by subsequent millennial-scale changes in the AMOC and its attendant effects on African (122) and Asian (127) monsoon systems and the position of the Intertropical Convergence Zone (147, 148) and North American storm tracks (72).

## Methods

**Data.** We compiled 166 published proxy records of either temperature (sea surface or continental) or precipitation for the 20- to 11-ka interval. We recalibrated the age models for all radiocarbon-based records whose raw data were available or could be obtained from the original author ( $n = 107$ ). For non-radiocarbon-based records (e.g., ice cores, speleothems, tuned records) and records with unavailable raw data, the published age models were used.

**Empirical Orthogonal Functions.** We use EOFs to provide an objective characterization of deglacial climate variability. Because the records used here are based on various proxies and thus have widely ranging variances in their original units, we standardized each one to zero mean and unit variance prior to calculating EOFs. This standardization causes each record to provide equal “weight” toward the EOFs. For the SST EOF analysis, records were kept in degrees Celsius and thus their original variance was preserved. Records were interpolated to 100-y resolution for all analyses.

**Modeling Records with Principal Components.** We model the proxy records as the weighted sum of the first two principal components from each regional EOF analysis to show how well the leading modes for each region represent the records. In other words, record  $x$  is modeled as  $PC1 \times EOF1_x + PC2 \times EOF2_x$ , where  $EOF_x$  is the loading for record  $x$ . We used a Monte Carlo procedure to derive error bars for the principal components shown in Figs. 4 and 5, which reflect uncertainties in the proxy records. The principal components

were calculated 1,000 times after perturbing the records with chronological errors, and in the case of calibrated proxy temperature records (e.g., Mg/Ca,  $U^{K}_{37}$ ), with random temperature errors as well. The standard deviation of these 1,000 realizations provides the  $1\sigma$  error bars for the principal components.

1. Monnin E, et al. (2001) Atmospheric CO<sub>2</sub> concentrations over the last glacial termination. *Science* 291:112–114.
2. Lemieux-Dudon B, et al. (2010) Consistent dating for Antarctic and Greenland ice cores. *Quat Sci Rev* 29:8–20.
3. Brook EJ, Harder S, Severinghaus J, Steig EJ, Sucher CM (2000) On the origin and timing of rapid changes in atmospheric methane during the last glacial period. *Global Biogeochem Cycles* 14:559–571.
4. Schilt A, et al. (2010) Glacial-interglacial and millennial-scale variations in the atmospheric nitrous oxide concentration during the last 800,000 years. *Quat Sci Rev* 29:182–192.
5. Broecker WS (1997) Thermohaline circulation, the Achilles heel of our climate system: Will man-made CO<sub>2</sub> upset the current balance. *Science* 278:1582–1588.
6. Clark PU, Pisias NG, Stocker TF, Weaver AJ (2002) The role of the thermohaline circulation in abrupt climate change. *Nature* 415:863–869.
7. Benway HM, Mix AC, Haley BA, Klinkhammer GP (2006) Eastern Pacific Warm Pool paleosalinity and climate variability: 0–30 kyr. *Paleoceanography* 21:PA3008.
8. Peeters FJC, et al. (2004) Vigorous exchange between the Indian and Atlantic oceans at the end of the past five glacial periods. *Nature* 430:661–665.
9. Hu AX, et al. (2010) Influence of Bering Strait flow and North Atlantic circulation on glacial sea-level changes. *Nat Geosci* 3:118–121.
10. Boyle EA, Keigwin L (1987) North Atlantic thermohaline circulation during the past 20,000 years linked to high-latitude surface temperature. *Nature* 330:35–40.
11. Curry WB, Oppo DW (2005) Glacial water mass geometry and the distribution of delta C-13 of Sigma CO<sub>2</sub> in the western Atlantic Ocean. *Paleoceanography* 20:PA1017.
12. Zahn R, et al. (1997) Thermohaline instability in the North Atlantic during meltwater events: Stable isotope and ice-rafted detritus records from core SO75-26KL. *Paleoceanography* 12:696–710.
13. Pahnke K, Goldstein SL, Hemming SR (2008) Abrupt changes in Antarctic Intermediate Water circulation over the past 25,000 years. *Nat Geosci* 1:870–874.
14. Roberts NL, Piotrowski AM, McManus JF, Keigwin LD (2010) Synchronous deglacial overturning and water mass source changes. *Science* 327:75–78.
15. Cao L, Fairbanks RG, Mortlock RA, Risk MJ (2007) Radiocarbon reservoir age of high latitude North Atlantic surface water during the last deglacial. *Quat Sci Rev* 26:732–742.
16. Robinson LF, et al. (2005) Radiocarbon variability in the Western North Atlantic during the last deglaciation. *Science* 310:1469–1473.
17. Mangini A, et al. (2010) Deep sea corals off Brazil verify a poorly ventilated Southern Pacific Ocean during H2, H1 and the Younger Dryas. *Earth Planet Sci Lett* 293:269–276.
18. Mix AC, et al. (1991) Carbon 13 in Pacific deep and intermediate waters, 0–370 ka: Implications for ocean circulation and Pleistocene CO<sub>2</sub>. *Paleoceanography* 6:205–226.
19. Pahnke K, Zahn R (2005) Southern Hemisphere water mass conversion linked with North Atlantic climate variability. *Science* 307:1741–1746.
20. Jung SJA, Kroon D, Ganssen G, Peeters F, Ganeshram R (2009) Enhanced Arabian Sea intermediate water flow during glacial North Atlantic cold phases. *Earth Planet Sci Lett* 280:220–228.
21. Muratli JM, Chasse Z, Mix AC, McManus J (2010) Increased glacial-age ventilation of the Chilean margin by Antarctic Intermediate Water. *Nat Geosci* 3:23–26.
22. Basak C, Martin EE, Horikawa K, Marchitto TM (2010) Southern Ocean source of 14C-depleted carbon in the North Pacific Ocean during the last deglaciation. *Nat Geosci* 3:770–773.
23. Behl RJ, Kennett JP (1996) Brief interstadial events in the Santa Barbara basin, NE Pacific, during the past 60 kyr. *Nature* 379:243–246.
24. Ortiz JD, et al. (2004) Enhanced marine productivity off western North America during warm climate intervals of the past 52 ky. *Geology* 32:521–524.
25. Broecker WS, et al. (1988) Comparison between radiocarbon ages obtained on coexisting planktonic foraminifera. *Paleoceanography* 3:647–657.
26. Skinner LC, Shackleton NJ (2004) Rapid transient changes in northeast Atlantic deep water ventilation age across Termination I. *Paleoceanography* 19:PA2005.
27. McManus JF, Francois R, Gherardi J-M, Keigwin LD, Brown-Leger S (2004) Collapse and rapid resumption of Atlantic meridional circulation linked to deglacial climate changes. *Nature* 428:834–837.
28. Gherardi JM, et al. (2009) Glacial-interglacial circulation changes inferred from Pa-231/Th-230 sedimentary record in the North Atlantic region. *Paleoceanography* 24:PA2204.
29. Hodell DA, Evans HF, Channell JET, Curtis JH (2010) Southern Ocean source of 14C-depleted carbon in the North Pacific Ocean during the last deglaciation. *Quat Sci Rev* 29:3875–3886.
30. Herguera JC, Jansen E, Berger WH (1992) Evidence for a bathyal front at 2000-M depth in the glacial Pacific, based on a depth transect on Ontong Java Plateau. *Paleoceanography* 7:273–288.
31. Matsumoto K, Oba T, Lynch-Stieglitz J, Yamamoto H (2002) Interior hydrography and circulation of the glacial Pacific Ocean. *Quat Sci Rev* 21:1693–1704.
32. Okazaki Y, et al. (2010) Deepwater formation in the North Pacific during the last glacial termination. *Science* 329:200–204.
33. Toggweiler JR (1999) Variation of atmospheric CO<sub>2</sub> by ventilation of the ocean's deepest water. *Paleoceanography* 14:571–588.

**ACKNOWLEDGMENTS.** We thank the National Oceanic and Atmospheric Administration Paleoclimatology program for data archiving, and the many scientists who generously contributed datasets used in our analyses. We also thank the National Science Foundation Paleoclimate Program and the Past Global Changes program for supporting the workshops that led to this synthesis.

34. Stephens BB, Keeling RF (2000) The influence of Antarctic sea ice on glacial-interglacial CO<sub>2</sub> variations. *Nature* 404:171–174.
35. Curry WB, Duplessy JC, Labeyrie LD, Shackleton NJ (1988) Changes in the distribution of delta 13C of Deep Water total CO<sub>2</sub> between the last glaciation and the holocene. *Paleoceanography* 3:317–341.
36. Zahn R, Mix AC (1991) Benthic foraminiferal  $\delta^{18}O$  in the ocean's temperature-salinity-density field: Constraints on Ice Age thermohaline circulation. *Paleoceanography* 6:1–20.
37. Adkins JF, McIntyre K, Schrag DP (2002) The salinity, temperature, and  $\delta^{18}O$  of the glacial deep ocean. *Science* 298:1769–1773.
38. Anderson RF, et al. (2009) Wind-driven upwelling in the Southern Ocean and the deglacial rise in atmospheric CO<sub>2</sub>. *Science* 323:1443–1448.
39. Marchitto TM, Lehman SJ, Ortiz JD, Fluckiger J, van Geen A (2007) Marine radiocarbon evidence for the mechanism of deglacial atmospheric CO<sub>2</sub> rise. *Science* 316:1456–1459.
40. Bryan SP, Marchitto TM, Lehman SJ (2010) The release of C-14-depleted carbon from the deep ocean during the last deglaciation: Evidence from the Arabian Sea. *Earth Planet Sci Lett* 298:244–254.
41. Rose KA, et al. (2010) Upper-ocean-to-atmosphere radiocarbon offsets imply fast deglacial carbon dioxide release. *Nature* 466:1093–1097.
42. De Pol-Holz R, Keigwin L, Southon J, Hebbeln D, Mohtadi M (2010) No signature of abyssal carbon in intermediate waters off Chile during deglaciation. *Nat Geosci* 3:192–195.
43. Broecker W (2009) The mysterious C-14 decline. *Radiocarbon* 51:109–119.
44. Skinner LC, Fallon S, Waelbroeck C, Michel E, Barker S (2010) Ventilation of the deep Southern Ocean and deglacial CO<sub>2</sub> rise. *Science* 328:1147–1151.
45. Jouzel J, et al. (2007) Orbital and millennial Antarctic climate variability over the past 800,000 years. *Science* 317:793–796.
46. Cuffey KM, et al. (1995) Large Arctic temperature change at the Wisconsin-Holocene glacial transition. *Science* 270:455–457.
47. Severinghaus JP, Brook EJ (1999) Abrupt climate change at the end of the last glacial period inferred from trapped air in polar ice. *Science* 286:930–934.
48. Grachev AM, Severinghaus JP (2005) A revised +10 + / - 4 degrees C magnitude of the abrupt change in Greenland temperature at the Younger Dryas termination using published GISP2 gas isotope data and air thermal diffusion constants. *Quat Sci Rev* 24:513–519.
49. Bender M, et al. (1994) Climate correlations between Greenland and Antarctica during the past 100,000 years. *Nature* 372:663–666.
50. Sowers T, Bender M (1995) Climate records covering the last deglaciation. *Science* 269:210–214.
51. Blunier T, et al. (1998) Asynchrony of Antarctic and Greenland climate change during the last glacial period. *Nature* 394:739–743.
52. Blunier T, Brook EJ (2001) Timing of millennial-scale climate change in Antarctica and Greenland during the last glacial period. *Science* 291:109–112.
53. Mix AC, Ruddiman WF, McIntyre A (1986) Late Quaternary paleoceanography of the tropical Atlantic, 1: Spatial variability of annual mean sea-surface temperatures, 0–20,000 years B.P. *Paleoceanography* 1:43–66.
54. Crowley TJ (1992) North Atlantic Deep Water cools the Southern Hemisphere. *Paleoceanography* 7:489–497.
55. Broecker WS (1998) Paleocirculation during the last deglaciation: A bipolar see-saw? *Paleoceanography* 13:119–121.
56. Morgan V, et al. (2002) Relative timing of deglacial climate events in Antarctica and Greenland. *Science* 297:1862–1864.
57. Rasmussen SO, et al. (2008) Synchronization of the NGRIP, GRIP, and GISP2 ice cores across MIS 2 and palaeoclimatic implications. *Quat Sci Rev* 27:18–28.
58. Steig EJ, et al. (1998) Synchronous climate changes in Antarctica and the North Atlantic. *Science* 282:92–95.
59. Brook EJ, et al. (2005) Timing of millennial-scale climate change at Siple Dome, West Antarctica, during the last glacial period. *Quat Sci Rev* 24:1333–1343.
60. Mulvaney R, et al. (2000) The transition from the last glacial period in inland and near-coastal Antarctica. *Geophys Res Lett* 27:2673–2676.
61. Stenni B, et al. (2011) Expression of the bipolar see-saw in Antarctic climate records during the last deglaciation. *Nat Geosci* 4:46–49.
62. Viau AE, Gajewski K, Sawada MC, Bunbury J (2008) Low- and high-frequency climate variability in eastern Beringia during the past 25 000 years. *Can J Earth Sci* 45:1435–1453.
63. Kurek J, Cwynar LC, Ager TA, Abbott MB, Edwards ME (2009) Late Quaternary paleoclimate of western Alaska inferred from fossil chironomids and its relation to vegetation histories. *Quat Sci Rev* 28:799–811.
64. Kokorowski HD, Anderson PM, Mock CJ, Lozhkin AV (2008) A re-evaluation and spatial analysis of evidence for a Younger Dryas climatic reversal in Beringia. *Quat Sci Rev* 27:1710–1722.
65. Williams JW (2003) Variations in tree cover in North America since the last glacial maximum. *Glob Planet Change* 35:1–23.
66. Williams JW, Shuman BN, Webb T, Bartlein PJ, Leduc PL (2004) Late-quaternary vegetation dynamics in north america: Scaling from taxa to biomes. *Ecol Monogr* 74:309–334.

67. Shuman B, Bartlein PJ, Webb T (2005) The magnitudes of millennial- and orbital-scale climatic change in eastern North America during the Late Quaternary. *Quat Sci Rev* 24:2194–2206.
68. Webb T, Anderson KH, Bartlein PJ, Webb RS (1998) Late Quaternary climate change in eastern North America: A comparison of pollen-derived estimates with climate model results. *Quat Sci Rev* 17:587–606.
69. Whitlock C (1992) Vegetational and climatic history of the Pacific Northwest during the last 20,000 years—implications for understanding present-day biodiversity. *Northwest Environ J* 8:5–28.
70. Grigg LD, Whitlock C, Dean WE (2001) Evidence for millennial-scale climate change during marine isotope stages 2 and 3 at Little Lake, western Oregon, USA. *Quat Res* 56:10–22.
71. Thompson RS, et al. (2004) Topographic, bioclimatic, and vegetation characteristics of three ecoregion classification systems in North America: Comparisons along continent-wide transects. *Environ Manage* 34:5125–148.
72. Wagner JDM, et al. (2010) Moisture variability in the southwestern United States linked to abrupt glacial climate change. *Nat Geosci* 3:110–113.
73. Asmerom Y, Polyak VJ, Burns SJ (2010) Variable winter moisture in the southwestern United States linked to rapid glacial climate shifts. *Nat Geosci* 3:114–117.
74. Shuman B, Bartlein PJ, Webb T, III (2005) The magnitudes of millennial- and orbital-scale climatic change in eastern North America during the Late Quaternary. *Quat Sci Rev* 24:2194–2206.
75. Thompson RS, Whitlock C, Bartlein PJ, Harrison SP, Spaulding WG (1993) Climatic changes in the western United States since 18,000 yr B.P. *Global Climates Since the Last Glacial Maximum*, eds HEJ Wright et al. (Univ Minnesota Press, Minneapolis), pp 468–513.
76. Bartlein PJ, et al. Pollen-based continental climate reconstructions at 6 and 21 ka: A global synthesis. *Clim Dynam* 37:775–802.
77. Shuman B, Newby P, Huang YS, Webb T (2004) Evidence for the close climatic control of New England vegetation history. *Ecology* 85:1297–1310.
78. Peteet D (2000) Sensitivity and rapidity of vegetational response to abrupt climate change. *Proc Natl Acad Sci USA* 97:1359–1361.
79. Yu SY, Berglund BE, Sandgren P, Lambeck K (2007) Evidence for a rapid sea-level rise 7600 yr ago. *Geology* 35:891–894.
80. Marlon JR, et al. (2009) Wildfire responses to abrupt climate change in North America. *Proc Natl Acad Sci USA* 106:2519–2524.
81. Reasoner MA, Jodry MA (2000) Rapid response of alpine timberline vegetation to the Younger Dryas climate oscillation in the Colorado Rocky Mountains, USA. *Geology* 28:51–54.
82. Stute M, et al. (1995) Cooling of tropical Brazil (5 °C) during the Last Glacial Maximum. *Science* 269:379–383.
83. Peterson LC, Haug GH, Hughen KA, Rohl U (2000) Rapid changes in the hydrologic cycle of the tropical Atlantic during the last glacial. *Science* 290:1947–1951.
84. Baker PA, et al. (2001) Tropical climate changes at millennial and orbital timescales on the Bolivian Altiplano. *Nature* 409:698–701.
85. Cruz FW, et al. (2005) Insolation-driven changes in atmospheric circulation over the past 116,000 years in subtropical Brazil. *Nature* 434:63–66.
86. Wang XF, et al. (2007) Millennial-scale precipitation changes in southern Brazil over the past 90,000 years. *Geophys Res Lett* 34:L23701.
87. Cruz FW, et al. (2009) Orbitally driven east-west antiphasing of South American precipitation. *Nat Geosci* 2:210–214.
88. Peterson LC, Haug GH, Hughen KA, Rohl U (2000) Rapid changes in the hydrologic cycle of the tropical Atlantic during the last glacial. *Science* 290:1947–1951.
89. Hodell DA, et al. (2008) An 85-ka record of climate change in lowland Central America. *Quat Sci Rev* 27:1152–1165.
90. Arz HW, Patzold J, Wefer G (1998) Correlated millennial-scale changes in surface hydrography and terrigenous sediment yield inferred from last-glacial marine deposits off northeastern Brazil. *Quat Res* 50:157–166.
91. Baker PA, et al. (2001) The history of South American tropical precipitation for the past 25,000 years. *Science* 291:640–643.
92. Fritz SC, Baker PA, Ekdahl E, Seltzer GO, Stevens LR (2010) Millennial-scale climate variability during the Last Glacial period in the tropical Andes. *Quat Sci Rev* 29:1017–1024.
93. Moreno PI, Lowell TV, Jacobson GL, Denton GH (1999) Abrupt vegetation and climate changes during the last glacial maximum and last termination in the Chilean Lake District: A case study from Canal de la Puntilla (41°). *Geogr Ann A* 81:285–311.
94. Heusser L, Heusser C, Mix A, McManus J (2006) Chilean and Southeast Pacific paleoclimate variations during the last glacial cycle: Directly correlated pollen and delta 18O records from ODP Site 1234. *Quat Sci Rev* 25:3404–3415.
95. Moreno PI, Leon AL (2003) Abrupt vegetation changes during the last glacial to Holocene transition in mid-latitude South America. *J Quat Sci* 18:787–800.
96. Haberle SG, Bennett KD (2004) Postglacial formation and dynamics of North Patagonian Rainforest in the Chonos Archipelago, southern Chile. *Quat Sci Rev* 23:2433–2452.
97. Muratli JM, Chase Z, McManus J, Mix A (2010) Ice-sheet control of continental erosion in central and southern Chile (36 degrees–41 degrees S) over the last 30,000 years. *Quat Sci Rev* 29:3230–3239.
98. Whitlock C, et al. (2006) Postglacial vegetation, climate, and fire history along the east side of the Andes (lat 41–42.5 degrees S), Argentina. *Quat Res* 66:187–201.
99. Markgraf V, Huber UM (2010) Late and postglacial vegetation and fire history in Southern Patagonia and Tierra del Fuego. *Palaeogeogr Palaeoclimatol Palaeoecol* 297:351–366.
100. Moreno PI, et al. (2009) Renewed glacial activity during the Antarctic cold reversal and persistence of cold conditions until 11.5 ka in southwestern Patagonia. *Geology* 37:375–378.
101. Berglund BE, Birks HJB, Ralska-Jasiewiczowa M, Wright HE, Jr., eds. (1996) *Palaeocological Events During the Last 15 000 Years—Regional Syntheses of Palaeocological Studies of Lakes and Mires in Europe* (Wiley, Chichester, UK) p 764.
102. Fletcher WJ, et al. (2010) Millennial-scale variability during the last glacial in vegetation records from Europe. *Quat Sci Rev* 29:2839–2864.
103. Elenga H, et al. (2000) Pollen-based biome reconstruction for southern Europe and Africa 18,000 yr BP. *J Biogeogr* 27:621–634.
104. Svenning JC, Normand S, Kageyama M (2008) Glacial refugia of temperate trees in Europe: Insights from species distribution modelling. *J Ecol* 96:1117–1127.
105. Wu HB, Guiot JL, Brewer S, Guo ZT (2007) Climatic changes in Eurasia and Africa at the last glacial maximum and mid-Holocene: Reconstruction from pollen data using inverse vegetation modelling. *Clim Dynam* 29:211–229.
106. Goni MFS, Turon JL, Eynaud F, Gendreau S (2000) European climatic response to millennial-scale changes in the atmosphere-ocean system during the last glacial period. *Quat Res* 54:394–403.
107. Fletcher WJ, Goni MFS (2008) Orbital- and sub-orbital-scale climate impacts on vegetation of the western Mediterranean basin over the last 48,000 yr. *Quat Res* 70:451–464.
108. Combourieu-Nebout N, et al. (2010) Rapid climate variability in the west Mediterranean during the last 25000 years from high resolution pollen data. *Clim Past* 5:503–521.
109. Renssen H, Isarin RFB (2001) The two major warming phases of the last deglaciation at similar to 14.7 and similar to 11.5 ka cal BP in Europe: Climate reconstructions and AGCM experiments. *Glob Planet Change* 30:117–153.
110. Atkinson TC, Briffa KR, Coope GR (1987) Seasonal temperatures in Britain during the past 22,000 years, reconstructed using beetle remains. *Nature* 325:587–592.
111. Lotter AF, et al. (2000) Younger Dryas and Allerod summer temperatures at Gerzensee (Switzerland) inferred from fossil pollen and cladoceran assemblages. *Palaeogeogr Palaeoclimatol Palaeoecol* 159:349–361.
112. Isarin RFB, Bohncke JJP (1999) Mean July temperatures during the Younger Dryas in northwestern and central Europe as inferred from climate indicator plant species. *Quat Res* 51:158–173.
113. Davis BAS, Brewer S, Stevenson AC, Guiot J, Data C (2003) The temperature of Europe during the Holocene reconstructed from pollen data. *Quat Sci Rev* 22:1701–1716.
114. Gasse F (2000) Hydrological changes in the African tropics since the Last Glacial Maximum. *Quat Sci Rev* 19:189–211.
115. Gasse F, Chalié F, Vincens A, Williams MAJ, Williamson D (2008) Climatic patterns in equatorial and southern Africa from 30,000 to 10,000 years ago reconstructed from terrestrial and near-shore proxy data. *Quat Sci Rev* 27:2316–2340.
116. Tjallingii R, et al. (2008) Coherent high- and low-latitude control of the northwest African hydrological balance. *Nat Geosci* 1:670–675.
117. Brown ET, Johnson TC, Scholz C, Cohen AS, King JW (2007) Abrupt change in tropical African climate linked to the bipolar seesaw over the past 55,000 years. *Geophys Res Lett* 34:L20702.
118. Castañeda IS, Werne JP, Johnson TC (2007) Wet and arid phases in the southeast African tropics since the Last Glacial Maximum. *Geology* 35:823–826.
119. Stager JC, Mayewski P, Meeker L (2002) Cooling cycles, Heinrich event I, and the desiccation of Lake Victoria. *Palaeogeogr Palaeoclimatol Palaeoecol* 183:169–178.
120. Barker P, Gasse F (2003) New evidence for a reduced water balance in East Africa during the Last Glacial Maximum: Implication for model-data comparison. *Quat Sci Rev* 22:823–837.
121. Garcin Y, Vincens A, Williamson D, Buchet G, Guiot J (2007) Abrupt resumption of the African monsoon at the Younger Dryas-Holocene climatic transition. *Quat Sci Rev* 26:690–704.
122. Tierney JE, et al. (2008) Northern Hemisphere controls on tropical southeast African climate during the past 60,000 years. *Science* 322:252–255.
123. Weldeab S, Lea DW, Schneider RR, Andersen N (2007) 155,000 years of West African monsoon and ocean thermal evolution. *Science* 316:1303–1307.
124. Mulitza S, et al. (2008) Sahel megadroughts triggered by glacial slowdowns of Atlantic meridional overturning. *Palaeoceanography* 23:PA4206.
125. Bonnefille R, Roeland JC, Guiot J (1990) Temperature and rainfall estimates for the past 40,000 years in equatorial Africa. *Nature* 346:347–349.
126. Powers LA, et al. (2005) Large temperature variability in the southern African tropics since the Last Glacial Maximum. *Geophys Res Lett* 32:L08706.
127. Wang YJ (2001) A high-resolution absolute-dated late Pleistocene monsoon record from Hulu Cave, China. *Science* 294:2345–2348.
128. Porter SC, An ZS (1995) Correlation between climate events in the North Atlantic and China during the last glaciation. *Nature* 375:305–308.
129. Sagawa T, Yokoyama Y, Ikehara M, Kuwae M (2011) Vertical thermal structure history in the western subtropical North Pacific since the Last Glacial Maximum. *Geophys Res Lett* 38:L00F02.
130. Thompson LG, et al. (1997) Tropical climate instability: The last glacial cycle from a Qinghai-Tibetan ice core. *Science* 276:1821–1825.
131. Yokoyama Y, et al. (2006) Dust influx reconstruction during the last 26,000 years inferred from a sedimentary leaf wax record from the Japan Sea. *Glob Planet Change* 54:239–250.
132. Herzschuh U (2006) Palaeo-moisture evolution in monsoonal Central Asia during the last 50,000 years. *Quat Sci Rev* 25:163–178.
133. Wang YJ, et al. (2008) Millennial- and orbital-scale changes in the East Asian monsoon over the past 224,000 years. *Nature* 451:1090–1093.
134. Schulz H, von Rad U, Erlenkeuser H (1998) Correlation between Arabian Sea and Greenland climate oscillations of the past 110,000 years. *Nature* 393:54–57.
135. Chen MT, et al. (2010) Dynamic millennial-scale climate changes in the northwestern Pacific over the past 40,000 years. *Geophys Res Lett* 37:L23603.



